communications chemistry

A Nature Portfolio journal

Article

https://doi.org/10.1038/s42004-025-01637-5

Cryo-EM structure of amyloid fibrils formed by full-length human αA-crystallin with pathogenic mutation R116C

Meinai Song, Jianting Han & Qin Cao ✉

The aggregation of crystallin proteins in human lens is the primary cause of cataracts, a disease that leads to blindness of tens of millions of people worldwide. Understanding the molecular architectures of these aggregated crystallin proteins can facilitate the development of therapeutic drugs to treat cataract without surgery. In this study, we prepared two types of crystallin fibrils, thick and thin, using recombinant human αA-crystallin harboring the disease-associated R116C mutation under neutral and acidic conditions, respectively. The structure of the thin fibrils was determined via cryo-EM at a resolution of 3.7 Å, whereas the thick fibrils appeared unsuitable for cryo-EM structure determination. Structure analysis suggests that the thin fibrils adopt a three-layered structure stabilized by extensive steric zipper interactions. The observation of aspartate and glutamate ladders stacking along the fibril axis is consistent with the preference for an acidic environment of the thin fibrils. Disease mutations on Arg49 and Arg54 appear to facilitate the fibril structure, suggesting the potential disease relevance of these fibrils. Taken together, our study provides the first near-atomic resolution structure of aggregated crystallin and may facilitate the future studies on the mechanism and therapeutic of cataracts.

To maintain the transparency of vertebrate eye lens, central lens cells undergo differentiation into fiber cells that eliminate organelles to minimize light scattering[1]. These fiber cells exhibit high expression of crystallin proteins, reaching concentrations of 250–400 mg/ml and constituting 90% of the total protein content[2]. Crystallin proteins must remain soluble throughout the lens's lifetime as fiber cells lack a protein degradation and replacement mechanism[3]. Accumulated protein damage induced by various factors such as UV radiation, oxidative stress, and mechanical injuries can lead to the aggregation of crystallin proteins. This aggregation contributes to lens opacity, serving as the primary cause of cataracts, the leading cause of blindness worldwide[3]. Hence, the inhibition of crystallin protein aggregation stands as a promising approach in the development of therapeutic or preventive drugs for cataracts.

The molecular mechanism of crystallin protein aggregation remains elusive. Recent studies suggest that the aggregated forms of crystallin proteins are amyloid fibrils. Reports indicate that human cataract lenses contain amyloids[4], and crystallin proteins are capable of forming fibrils both in vitro and in vivo[5,6]. Amyloid-β aggregates were detected in the lenses of Alzheimer's disease patients, and amyloid-β may promote the amyloid formation of crystallin proteins[5]. In this study, we present the first, to our knowledge, high-resolution structure of crystallin fibrils form – the cryo-EM structure of human αA-crystallin harboring the pathological R116C mutation formed in vitro, determined at a resolution of 3.7 Å. αA-crystallin is a major constituent of crystallin protein family, which are composed of α-, β-, and γ-crystallins. Our findings provide valuable insights for the pathogenic and therapeutic investigations of cataracts.

Results

Fibril formation and stability of recombinant αA-crystallin

We selected a disease variant of αA-crystallin (R116C) to generate fibrils due to its association with a subtype of autosomal dominant cataracts[7]. Fibrils were prepared following established protocols[6,8]: purified αA-crystallin R116C proteins underwent incubation in either neutral or acidic buffers (pH 7.4 with guanidine hydrochloride or pH 2.0 with trifluoroethanol, see Methods) and were subjected to a 2-hour incubation at 60 °C. Subsequent observation of the fibrils via negative stain electron microscopy revealed that those grown under neutral conditions exhibited greater thickness compared to those grown under acidic conditions (Fig. 1a). The ensuing discussion will distinguish between these two types of fibrils as "thick fibrils" and "thin fibrils," both of which were utilized for cryo-EM structure determination.

Bio-X Institutes, Key Laboratory for the Genetics of Developmental and Neuropsychiatric Disorders, Ministry of Education, Shanghai Jiao Tong University, Shanghai, China. ✉e-mail: caoqin@sjtu.edu.cn

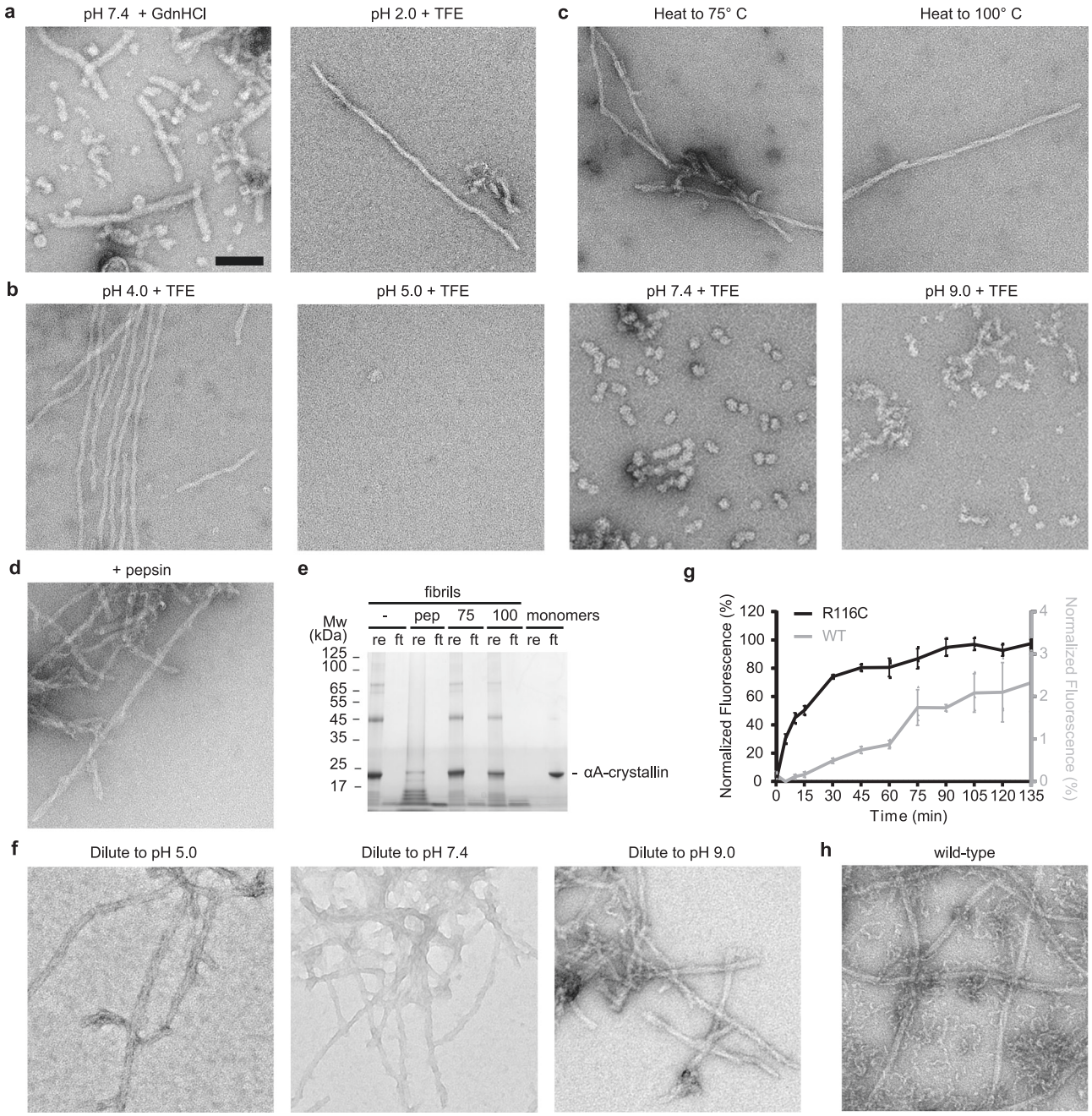

Fig. 1 | Fibril formation and stability of αA-crystallin fibrils. a Negative stain EM images of thick fibrils formed under neutral conditions (left) and the thin fibrils formed under acidic conditions (right). GdnHCl, guanidine hydrochloride; TFE, trifluoroethanol. Scale bar = 100 nm. **b** Negative stain EM images of αA-crystallin incubated in the same buffer of the thin fibrils with pH levels adjusted. **c**–**d**, **f** Negative stain EM images of the thin fibrils heated (**c**), incubated with pepsin (**d**), or diluted to buffers with indicated pH (f). **e** SDS-PAGE of samples filtered with 0.1 μm filters. re, retained fraction; ft, flowthrough fraction, -, no treatment; pep, incubated with pepsin; 75, heated to 75 °C; 100, heated to 100 °C. **g** ThT curves of αA-crystallin wild type (grey) and R116C (black). Data are shown as mean± s.d., $n = 3$ independent experiments. **h**, Negative stain EM image of fibrils formed by wild-type αA-crystallin.

In addition to the growth conditions described above, αA-crystallin R116C proteins were also subjected to incubation in a buffer akin to that used for thin fibril preparation, but with pH levels adjusted within the range of 4.0 to 9.0. Thin fibrils were observed in buffers with a pH of 4.0, while no formation occurred at pH levels of 5.0 and above (Fig. 1b), indicating that the generation of these thin fibrils prefers an acidic environment.

Cryo-EM structure determination of αA-crystallin fibrils

Cryo-EM dataset was collected for both the thick fibrils formed under neutral conditions and the thin fibrils formed under acidic condition. Upon examination of the Cryo-EM images, we observed distinct morphologies for these two types of fibrils (Supplementary Fig. 1a). During 2D classification of the thick fibrils, we found that nearly all particles were grouped into a single 2D class that appears fuzzy and lacks distinctive features (Supplementary Fig. 1b). The morphology of this 2D class indicated an absence of a regular structure in these fibrils, making them unsuitable for Cryo-EM structure determination.

Conversely, in the 2D classifications of the thin fibrils, we identified recognizable classes belonging to a twisted fibril species with a width of 110 Å and a cross-over distance of 481 Å (Supplementary Fig. 1c, Supplementary Fig. 2, Supplementary Fig. 3). We determined the 3D structure of

Table 1 | Cryo-EM data collection, refinement and validation statistics of the thin αA-crystallin fibrils

	αA-crystallin (EMD-63849, PDB 9U4L)
Data collection and processing	
Magnification	×130,000
Voltage (kV)	300
Electron exposure ($e^-/Å^2$)	40
Defocus range (μm)	0.8–3.5
Pixel size (Å)	0.932
Symmetry imposed	C_1
Helical rise (Å)	4.78
Helical twist (°)	−1.79
Initial particle images (no.)	3,237,381
Final particle images (no.)	58,325
Map resolution (Å)	3.7
FSC threshold	0.143
Map resolution range (Å)	200–3.7
Refinement	
Initial model used (PDB code)	De novo
Model resolution (Å)	4.1
FSC threshold	0.5
Model resolution range (Å)	200–4.1
Map sharpening *B* factor ($Å^2$)	149
Model composition	
Nonhydrogen atoms	3462
Protein residues	414
Ligands	0
B factors ($Å^2$)	
Protein	107.5
Ligand	–
R.m.s. deviations	
Bond lengths (Å)	0.003
Bond angles (°)	0.556
Validation	
MolProbity score	2.02
Clashscore	9.5
Poor rotamers (%)	0
Ramachandran plot	
Favored (%)	91.04
Allowed (%)	8.96
Disallowed (%)	0

this species at a resolution of 3.7 Å, revealing a three-layered fibril core and additional densities that potentially represent extended fibril core regions (Supplementary Fig. 1d&e, Supplementary Fig. 4, extra densities are indicated with arrows). Atomic model was built into the cryo-EM map unambiguously using the amino acid sequence of αA-crystallin, and the structure determination and model building statistics are listed in Table 1. The data processing workflow of the thin fibrils is illustrated in Supplementary Fig. 2.

The overall structure of the thin fibrils

The fibril core consists of residues 21-89 of αA-crystallin that form eight β-strands interconnected by loops (Fig. 2a, b). Notably, the pathological mutation R116C is located outside this core region (Fig. 2a), indicating that it does not promote fibril formation via favoring the formation of the fibril core observed here (see discussion). The fibril core adopts a three-layered fold containing two hollow cavities within the core (Fig. 2b, c). These cavities primarily result from the positioning of the kink between β4 and β5 against the unkinked β7 stand (Fig. 2b–d).

In the fibril core, we observed eight positively charged residues and eleven negatively charged residues, some of which (e.g., Glu33 and Asp35) do not engage in salt bridge formation to neutralize the electrostatic repulsion during fibril stacking (Fig. 2c). This observation is consistent with the finding that these fibrils only form under acidic conditions (see discussion). Additionally, we found that a large number of hydrophobic residues orient away from the interior of the fibril cores, rather than facing inward to form hydrophobic cores. We note that this observation does not necessarily suggest that these hydrophobic residues do not contribute to the stability of the fibrils, as many of these residues are shielded by the extended fibril core indicated by the fuzzy coat in the cryo-EM map (see descriptions below).

Steric zippers in the fibril structure

The interlayer stacking of the thin fibrils is stabilized by the arrangement of eight β-strands into eight parallel β-sheets (Fig. 2). The fibril core is further stabilized by steric zipper interactions between these β-sheets (Fig. 3). Specifically, β2 interacts with β3 through hydrogen bonds formed between Thr43, Ser45, and Glu33; β1 interacts with β4 and β5 through salt bridges between Glu29, Arg49, and Arg54 along with hydrophobic interactions between Phe27 and Val56; β3 interacts with β8 through hydrophobic interactions among Ile44, Val87, and Val89; and the kink between β3 and β4 interacts with β7 through hydrophobic interactions among Phe53, Ile73, and Leu75 (Fig. 3). These interactions unite various β-sheets, thereby stabilizing the fibril structure.

When viewed along the filament axis, it becomes apparent that each layer of the thin fibrils is not flat, leading to interlayer sidechain interactions in most steric zippers (Fig. 2d). Specifically, β1 from layer i interacts with β4 and β5 from the layer i-1; β3 from layer i interacts with β8 from layer i+2; and the kink between β4 and β5 from layer i interacts with β7 from layer i+1 (Fig.3). This intertwined stacking pattern is a common feature in amyloid fibrils and may enhance the kinetics of fibril growth and nucleation[9,10].

Stability assays of the thin fibrils

To assess the durability of the thin fibrils, pre-existing thin fibrils underwent exposure to temperatures of 75 °C or 100 °C, as well as incubation with pepsin. Following these procedures, we noted that the fibrils maintained a comparable morphology and quantity to samples that received no treatment (Fig. 1c, d). To further compare the quantity of αA-crystallin fibrils before and after treatment, we filtered the samples with a 0.1 μm filter and analyzed the retained and flowthrough fractions using SDS-PAGE (see Methods). The results indicated that pre-formed thin fibrils, with or without treatment, were all retained by the filter (Fig. 1e, Supplementary Fig. 5). In contrast, αA-crystallin monomers could not be retained by the filter and were present in the flowthrough fraction (Fig. 1e, Supplementary Fig. 5). This observation suggests that thin fibrils exhibited resilience against harsh conditions such as high temperatures and proteolytic cleavage, indicating their stability and implying that their formation is irreversible. In addition, we observed that after treatment with pepsin, a significant portion of αA-crystallin was digested into smaller fragments (Fig. 1e, Supplementary Fig. 5), suggesting that the fibril core region, rather than other regions, is resistant to proteolytic cleavage when forming fibrils.

To further explore the thin fibrils' sensitivity to pH variations, pre-formed fibrils were diluted threefold (v/v) into the same buffer with pH adjustments. We found that the fibrils retained similar morphology and quantity as those diluted into the unaltered buffer (Fig.1f). These findings suggest that while the growth of thin fibrils prefers an acidic environment, pre-formed fibrils exhibit resistance to changes in pH.

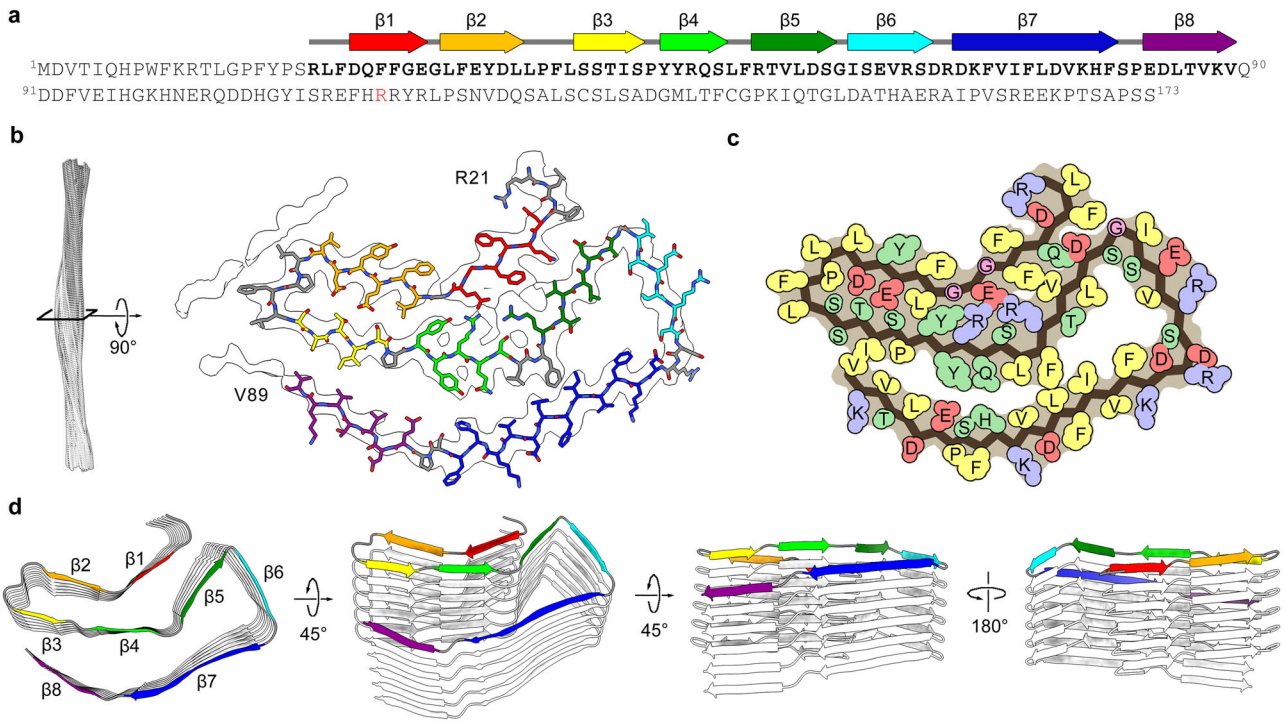

Fig. 2 | Cryo-EM structure of the thin fibrils. a Amino acid sequence of αA-crystallin aligned with the secondary structure schematic of the fibril core. Bold labels indicate residues resolved in the fibril core; Arg116 (mutated to cystine in this study) is highlighted in red. **b** Side view of the fibril reconstruction (left) and a cross-sectional layer showing the cryo-EM density map with overlaid atomic model (right). The model is colored to match the schematic in (**a**). **c** Space-filling model of the fibril core. Residues are color-coded: hydrophobic (yellow), hydrophilic (green), negatively charged (red), and positively charged (blue). **d** Cartoon representation of the fibril structure with six stacked layers. The top layer is colored as the schematic in (**a**).

Comparison of fibril formation of wildtype and R116C αA-crystallin

To investigate the influence of the point mutation R116C on the formation of thin fibrils, we purified wild-type αA-crystallin and prepared fibrils in parallel to αA-crystallin R116C. Thioflavin T (ThT) assays indicated that both samples exhibited the typical kinetic curve of amyloid fibril formation (Fig. 1g). A comparison of the kinetic curves suggested that αA-crystallin R116C forms fibrils faster than the wild type (Fig. 1g, Supplementary Data 1), indicating that R116C facilitates the fibril formation of αA-crystallin. The fluorescence reading of αA-crystallin R116C is much stronger than that of the wild type (Fig. 1g, Supplementary Data 1), suggesting that the wild-type αA-crystallin may not form identical fibrils as R116C. Negative stain EM revealed that while fibrils with a morphology comparable to the thin fibrils formed by αA-crystallin R116C were observed in the wild-type sample, a thinner and more bent fibril species was also present (Fig. 1h), which may account for the distinct ThT readings in both samples. Further studies are required to determine the structure of wild type αA-crystallin fibrils and compare them with the R116C structure reported here.

Comparison of the native fold and fibril structure of αA-crystallin

In its native conformation, αA-crystallin exists as a highly soluble large complex with αB-crystallin[11]. The pivotal point in the aggregation process lies in the disruption of this native conformation. Here, we compared the native fold of αA-crystallin with its fibril structure determined in this study. Due to the unavailability of a high-resolution structure of the native αA-crystallin form, we utilized a model generated through a combination of homology modeling, NMR spectroscopy, and low-resolution cryo-EM map fitting (PDB ID 6T1R[11]), along with the prediction from AlphaFold 3 to represent the native form of αA-crystallin. Upon coloring these native models using the same color scheme as in Fig. 2a, we observed that the residues constituting β1-5 in the fibril structure are located within the N-terminal flexible region in the native fold, which lacks distinct secondary structures (Supplementary Fig. 6). In contrast, the residues forming β6-8 in the fibril structure are located in the central core domain of the native fold, characterized by well-ordered β-strands. Additionally, these residues also form three β-strands in the native fold, exhibiting a similar residue range for each strand (Supplementary Fig. 6). These findings suggest that the exposure of residues within β6-8 may serve as the initial trigger for the formation of the thin fibrils.

Extra densities suggest an extended fibril core of αA-crystallin

Aside from the clearly defined fibril core, we have identified additional densities surrounding the core (Supplementary Fig. 1d, Supplementary Fig. 4). These densities appear fragmented and lack sufficient detail to construct a reliable model. Lowering the threshold in the map display reveals a potential connection between these extra densities and the main chain of the existing fibril core (Supplementary Fig. 4), indicating a probable extension of the fibril core. Specifically, the current fibril core shows potential for extension on both its N- and C-termini, thus forming an elongated fibril core (Fig. 4a). Due to the limited quality of these extra densities, we are unable to ascertain the exact range and registration of residues belong to the extended regions. Based on the length of these densities, we tentatively estimate the residue range of the extended fibril core to be approximately residues 12-117 (Fig. 4b). These extended regions could potentially enhance the stability of the thin fibrils as they may shield certain outward-facing hydrophobic residues within the current fibril core from solvent exposure (Figs. 2c and 4a). It is important to acknowledge that, at this stage, we cannot definitively rule out the possibility that these extra densities originate from the residues belonging to an extra polypeptide chain.

Discussion

To date, the primary treatment for cataracts involves the surgical removal of the opaque lens, as there are currently no effective drugs available for preventing or treating cataracts[3]. Despite the high success rate of cataract surgery, there is ongoing interest in pharmacological treatment for cataracts

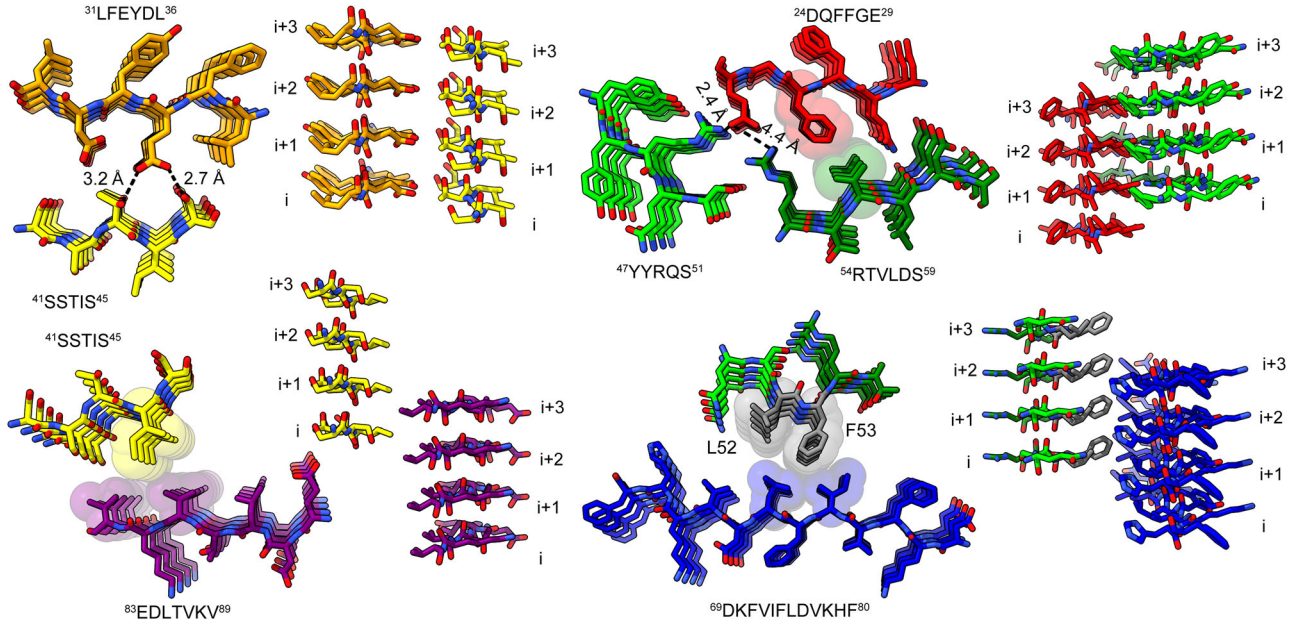

Fig. 3 | Steric zipper interactions that stabilize the fibril core. β-strands from four stacked layers (i, i + 1, i + 2, and i + 3) are shown in sticks and colored according to the schematic in Fig. 2a. Dashed black lines indicate the distance between atoms, and residues involved in hydrophobic interactions are displayed as spheres.

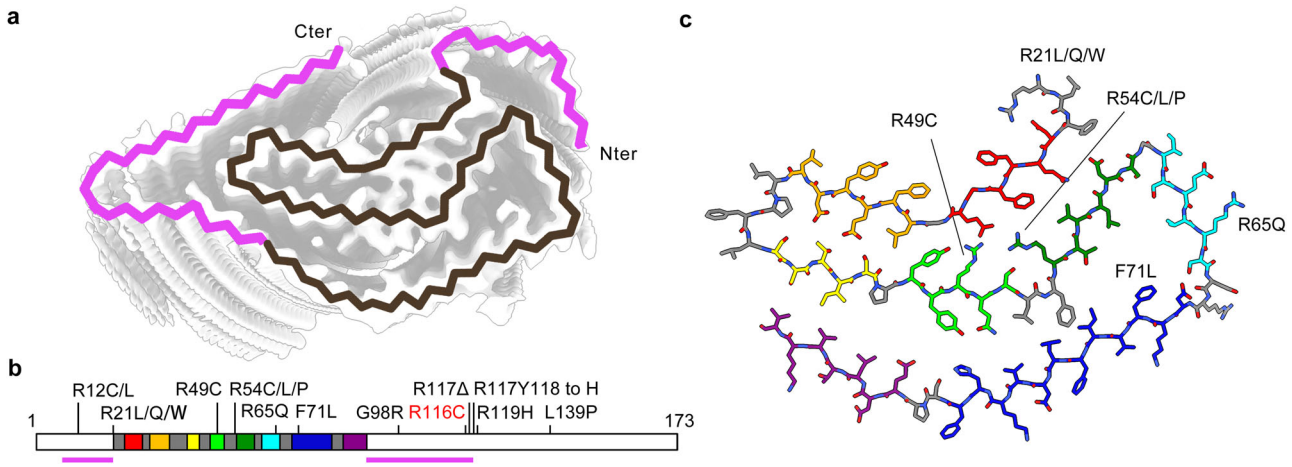

Fig. 4 | Mapping pathogenic mutations on the αA-crystallin fibril core. a The extended fibril core of αA-crystallin. The cryo-EM map of αA-crystallin fibrils, displayed with a low threshold and in transparency, is overlaid with a zigzag line representing the main chain of αA-crystallin. Residues resolved in fibril core are colored brown, while those with electron densities visible only at a low threshold are colored pink. **b** Schematic representation of full-length αA-crystallin. The fibril core determined in this study is colored according to the schematic in Fig. 1a, and the extended fibril core hypothesized in (**a**) is represented as pink lines. Reported pathogenic mutations of αA-crystallin are labeled, with R116C highlighted in red. **c**, Atomic model of the αA-crystallin fibril core with pathogenic mutations labeled.

due to surgery risk and limited access to surgical facilities in the developing world. Inhibiting crystallin aggregation is a promising strategy in developing prevention methods for cataract, and understanding the molecular architecture of crystallin aggregation is the key to this strategy. In this study, we prepared fibrils using αA-crystallin, a major constituent of the crystallin protein family that is present in high concentrations within human lenses. We generated these fibrils under two previously reported conditions - one at neutral pH and the other at acidic pH - which yielded two distinct fibril morphologies: thick and thin fibrils (Fig. 1a). We attempted to determine the cryo-EM structure of both fibril types, and successfully determined the structure of the thin fibrils at a resolution of 3.7 Å. Unfortunately, the thick fibrils were found to be unsuitable for structure determination during cryo-EM data processing, likely due to a lack of regular fibril structure. It remains unclear whether this irregular structure was caused by damage incurred during sample preparation, such as incubation with GdnHCl, or if it reflects an intrinsic property of this particular fibril type. Nevertheless, our study reports the first near-atomic-resolution structure of crystallin fibrils, which may potentially provide valuable insights into the molecular mechanisms underlying crystallin aggregation in cataract lenses.

It is important to acknowledge that due to the polymorphism of amyloid fibrils, the fibrils prepared in vitro may not have the same structure as those formed in the patients' tissues[12]. For instance, previous research has demonstrated that fibrils formed by α-synuclein[13], TDP-43[14], and Aβ[15] in vitro exhibit different structures compared to those formed in patients' brains. To date, only pathological tau fibrils have been successfully reproduced in vitro[16]. Therefore, it is possible that the fibril structure we reported here may not represent the pathological states of αA-crystallin in cataract. Extracting fibrils from cataract lenses and determining their structures should be a better method to investigate the pathological conformation of crystallin. However, current cataract surgery mostly removes cataract lenses through phacoemulsification, which may lead to the disruption of the regular polymer structures in the cataract lenses, raising the difficulties of

ex vivo structure determination of cataract aggregates. Despite these challenges, studies have shown that under certain conditions, in vitro formed amyloid fibrils can reproduce the same structure found in patients' tissues[16,17]. Additionally, the partial structural similarity between in vitro and ex vivo fibrils enables researchers to use in vitro fibrils to develop tracers targeting the pathological fibrils[18]. These findings suggest that determining the structure of in vitro formed fibrils is still valuable, as they may partially or fully reproduce the pathological structure. Further studies are required to examine the disease relevance of the fibril structure reported here, such as developing specific tracers of the thin fibrils through structure-based rational design and testing their effect on cataract lenses.

Crystallin proteins are highly soluble and thermodynamically stable to maintain transparency in the human lens over a lifetime. Therefore, harsh conditions must be used to disrupt their native fold and trigger aggregation in vitro. These treatments are believed to mimic the long-term damage of crystallin proteins accumulated over decades and accelerate the protein aggregation process in the test tube. In the fibril structure we observed, we found many glutamate and aspartate "ladders" packed along the fibril axis, with no nearby positively charged residues to balance their negative charges, including Glu33, Asp35, Asp69, Glu83, and Asp84. These observations suggest that the thin fibrils prefer acidic growth conditions, as protonation of the glutamate and aspartate sidechains under acidic pH would eliminate their negative charges. This would prevent destabilizing electrostatic repulsions within the packed acidic residue ladders. Consistent with this, we found that the thin fibrils exclusively grow in acidic pH conditions in vitro (Fig. 1b). This raises the question of whether this same fibril structure can actually be formed in cataract lenses, which have a more neutral physiological pH.

Previous studies suggest the pH in lens fiber cells is around 6.5[19], and these cells lack organelles like lysosomes, which means there may not be a sufficiently acidic environment in the fiber cells to favor the formation of the thin fibrils observed in vitro. However, we cannot exclude the possibility that the accumulated protein damage in the lens may cause the aspartate and glutamate residues to lose their negative charge. For example, it is known that aspartate and glutamate residues can be decarboxylated by radiation damage during X-ray diffraction experiments[20]. It is plausible that long-term light-induced damage could cause a similar effect. Additionally, light exposure can generate reactive oxygen species (ROS) that further damage lens proteins[21]. ROS-induced modifications, including oxidation of cysteine, methionine, and tryptophan residues, are considered a hallmark of cataract[22]. Further studies are needed to investigate whether aspartate and glutamate residues are also affected by ROS in cataract. Alternatively, the thin fibrils could potentially form in the lens through a short-term micro-environmental pH variation, potentially caused by ROS or other factors. These fibrils are irreversible and resistant to neutral pH (as shown in Fig. 1f), and may serve as seeds to facilitate the aggregation of other αA-crystallin proteins. In this case, the unsatisfied steric zipper interaction pairs caused by the non-flat fibril layers may be responsible for recruiting soluble proteins to add as new layers, leading to further fibril growth.

To investigate how disease mutations in αA-crystallin impact the fibril structure determined in this study, we annotated all known mutations on the αA-crystallin sequence (Fig. 4b). These mutations can be divided into three groups based on their respective locations: (i) those located within the central fibril core region (e.g., R49C, R65Q), (ii) mutations located outside the fibril core but within the extended fibril core region (e.g., R12C, G98R), and (iii) mutations located on the periphery or outside the extended fibril core region (e.g., R116C, L139P). Upon a closer examination of the fibril structure, we discovered that two mutation sites, Arg49 and Arg54, are actively involved in direct interactions within the fibril structure, unlike other sites in the first category (Fig. 4c). These two arginine residues engage in salt bridges with Glu29, resulting in an imbalance of charges with two positively charged and one negatively charged residues. The imbalance is exacerbated, particularly considering the potential protonation of the glutamate during acidic conditions. Moreover, the size of these two arginine residues and one glutamate residue leads to overcrowding in this region, necessitating the main chain of Gly28 to bend to accommodate this tight packing. Mutations at these two arginine sites (R49C, R54C, R54L, and R54P) all lead to a decrease in positive charge and reduction in side chain size. This adjustment should promote the stability of the fibril structure by balancing the net charge and alleviating overcrowding. Collectively, our structure analysis suggested that the pathological mutations R49C, R54C, R54L, and R54P may potentially facilitate the formation of the thin fibril structure, which partially support the disease relevance of this fibril conformation. These mutations may cause autosomal dominant cataract by lowering the energy barrier for the formation of these thin fibrils. In contrast, other disease mutations, such as R116C (the one harbored by the protein used in this study), do not influence the structure core of the fibril. Therefore, the question of how these mutations facilitate the fibril formation of αA-crystallin remains elusive. It is worth noting that a mutation can drive fibril formation even if it is not present in the core of the fibril. Additionally, these other mutations could potentially exacerbate cataract pathogenesis through alternative mechanisms, such as favoring the formation of different fibril structures or destabilizing the native fold of αA-crystallin.

In summary, we reported the near-atomic resolution structure of amyloid fibrils formed by recombinant human αA-crystallin with the pathological mutation R116C. Our structure offers molecular-level evidence demonstrating the capacity of crystallin proteins to form amyloid fibrils. Furthermore, it provides us with the initial insight into the potential molecular architecture of the aggregated crystallin proteins in cataract lenses. These finding sheds new light on the mechanical and therapeutical investigations of cataracts.

Methods

Protein expression and purification

The full-length human αA-crystallin, either wild type or carrying the pathological mutation R116C, was expressed and purified according to a previously reported protocol with minor adjustments[23]. Briefly, the c-terminal His-tagged protein was expressed in *Escherichia coli* BL21(DE3) cells using the pET-28b(+) vector. Cells cultures were grown at 37 °C to an OD600 of 0.6–0.8, then cultured at 30°C for an additional 18 hours upon induction with 0.4 mM IPTG. Subsequent to incubation, the cells were harvested by centrifugation at 5500 × *g* for 20 min and subjected to sonication in a lysis buffer (50 mM sodium phosphate pH 7.4, 300 mM NaCl, 5% glycerol, 10 mM imidazole). Following centrifugation at 21,000 × *g* for 45 minutes at 4 °C, cellular debris was removed from the lysate. The soluble fractions were loaded to Ni-NTA resin, and the desired proteins were eluted with the lysis buffer containing 200 mM imidazole. We found that the eluted proteins are prone to precipitate during the concentrating step, likely because they are not properly folded. To refold the proteins, the eluted protein solution was mixed with urea to a final concentration of 3 M and subsequently dialysis against a refolding buffer (50 mM sodium phosphate pH 7.4, 150 mM NaCl) overnight to remove the urea.

Fibril preparation and stability assays

The purified αA-crystallin R116C proteins were diluted to a concentration of 80 μM in two distinct buffer solutions. The first buffer comprised 50 mM sodium phosphate at pH 7.4, 150 mM NaCl, supplemented with 1 M guandidine hydrochloride (GdnHCl), while the second buffer contained 50 mM sodium phosphate at pH 2.0, 150 mM NaCl, and 10% (v/v) trifluoroethanol (TFE). The protein solutions in both buffers were incubated at 60 °C for 2 hours to facilitate fibril formation. Notably, the first buffer yielded thick fibrils, whereas the second buffer led to the generation of thin fibrils. In addition, αA-crystallin R116C proteins were diluted to 80 μM in the second buffer with pH adjustments to 4.0, 5.0, 7.4, and 9.0, respectively, followed by a 2-hour incubation at 60 °C. Fibrils grown in the first buffer (pH 7.4) and the second buffer (pH 2.0) were used for cryo-EM structure determination.

To assess the stability of the thin fibrils, pre-existing fibrils (prepared in the second buffer) were diluted threefold (v/v) with the same buffer, but with

pH modifications to 5.0, 7.4, and 9.0. The pH change of mixed solutions was confirmed by pH test paper, and the mixtures were then incubated at room temperature for 20 minutes and subsequently examined using TEM. Additionally, pre-formed thin fibrils were heated at 75 °C or 100 °C for 15 minutes, as well as incubated with 0.1 mg/ml pepsin for 1 hour and then analyzed under TEM. All fibril preparation and stability assays were performed within Eppendorf tubes.

Quantification assays for fibril stability

Pre-formed thin fibrils were heated at 75 °C or 100 °C for 15 minutes, as well as incubated with 0.1 mg/ml pepsin for 1 hour. Thin fibrils without treatment and αA-crystallin R116C proteins without incubation in the fibril growth condition were also analyzed as controls. The samples were filtered with 0.1 μm centrifugal filters (Millipore). The flow-through fraction was collected, and the retained fraction was mixed with the same buffer used for fibril growth in an equal volume to the unfiltered sample. Both factions were analyzed with SDS-PAGE. To aid the separation of αA-crystallin aggregates into monomers on SDS-PAGE, the retained factions were mixed with 9-fold (v/v) of hexafluoroisopropanol (HFIP) and incubated for 5 hours. HFIP was then evaporated, and the remaining solution was mixed with SDS loading buffer. The SDS-PAGE gels were visualized with Coomassie staining.

Thioflavin T (ThT) assays

The purified αA-crystallin wild-type or R116C proteins were diluted to a concentration of 80 μM in 50 mM sodium phosphate at pH 2.0, 150 mM NaCl, 10% (v/v) TFE, and 30 μM ThT. The samples were incubated at 60 °C for 2 hours, and 80 μl aliquots were pipetted from the same solution at 0, 5, 10, 15, 30, 45, 60, 75, 90, 105, 120 and 135 minutes for fluorescence readings. Each aliquot was transferred to a 96-well plate, and the ThT fluorescence was measured using a FLUOstar Omega plate reader (BMG LABTECH) with excitation and emission wavelengths of 440 nm and 480 nm, respectively. The fluorescence curves were averaged from three independent replicates. The fluorescence values were normalized to set the maximum value to 100% and the minimum value to 0%. The fluorescence values of wild-type and R116C αA-crystallin were normalized to the same set of maximum and minimum values.

Cryo-EM data collection and processing

For both the thick and thin fibrils, 3 μl of fibril samples were applied to a holey carbon film (Quantifoil 1.2/1.3, 200 mesh) and incubated for 2 minutes. The grids were blotted with filter paper for 5 seconds and plunge-frozen in liquid ethane using a Vitrobot Mark IV (Thermo Fisher Scientific). Data were collected on a FEI Titan Krios G3i transmission electron microscope (Thermo Fisher Scientific) operated at 300 kV with a Falcon 4i detector in counting mode. The total accumulated dose was 40 $e^-/Å^2$ per image, and the nominal physical pixel size was 0.932 Å/pixel. A total of 3057 and 5909 micrographs were collected for the thick and the thin fibrils, respectively.

Data processing of the thin fibrils followed the workflow outlined in Supplementary Fig. 1. Motion correction and contrast transfer function (CTF) estimation were performed using MotionCor2[24] and CTFFIND-4.1.827[25], respectively. Helical reconstruction was carried out using RELION 4.0[26]. Particles were automatically picked with Topaz v0.2.5[27] and extracted at box sizes of 720 and 360 pixels, respectively. The inter-particle distance was maintained at 10% of the box size. Two-dimensional (2D) classification of particles with a 720-pixel box size was performed, and only one fibril morphology was observed from the 2D classes, along with other classes representing damaged, bundled, or unrecognizable particles. High-quality 2D classes from the identified morphology were selected for initial 3D reconstruction. The helical symmetry parameters were determined as follows: the 2D classes were stitched together to encompass a full cross-over of the fibrils, with the cross-over distance measuring approximately 480 Å (as shown in Supplementary Fig. 1C, representing the rise value corresponding to a twist value of 180°). The helical rise was established at 4.8 Å through the examination of the power spectrum of the 2D classes (Supplementary Fig. 1C, it is also a common feature of amyloid fibrils). The helical twist was calculated as 180° × helical rise ÷ cross-over distance, resulting in a value of 1.8°. The helical twist was then set to −1.8° because the left-handed twist is assumed for these fibrils, as the left-handed twist is more common for amyloid fibrils. We acknowledge that we cannot confirm the handedness of the fibrils at the current stage, and the selection of handedness should not affect the monomer structure of the fibrils. Helical symmetry was refined during subsequent 3D reconstructions. After the generation of the initial map, 2D classification of particles with a 360-pixel box size was performed, and particles belonging to the same fibril morphology were selected for 3D classification with the initial map as a reference. Three additional rounds of 3D classification were performed to select the best particles. In each round, the map from the best 3D class of the prior round was used as the initial reference. The final selected particles were used for another round of 3D reconstruction to refine the helical symmetry parameters. The search range for helical twist was set from −1.9° to −1.7° with the search step of 0.01°, whereas the search range for helical rise was set from 4.7 Å to 4.9 Å with the search step of 0.05 Å. The refined helical twist was −1.79°, and the refined helical rise was 4.78 Å. Finally, the golden-standard 3D refinement was performed using the best particles and the refined helical symmetry parameters. A map with a resolution of 3.7 Å was generated, and further refinement with CTF refinement and Bayesian polishing did not improve this map. Therefore, this map was used as the final map for the following model building. The resolution was estimated using the 0.143 Fourier shell correlation (FSC) resolution cutoff.

Data processing for the thick fibrils followed a similar approach as described above. Motion correction and CTF estimations were performed, and particles were automatically picked with a box size of 360 pixels. Subsequent 2D classification revealed that almost all particles were grouped into a single 2D class without clear features (Supplementary Fig. 1b). This observation typically indicates that these fibrils are unsuitable for Cryo-EM structure determination, possibly due to the lack of a regular structure. No further data processing was pursued for this thick fibril species. In addition to the thick fibrils, we also observed a thin fibril species with a width of ~2 nm in this dataset (Supplementary Fig. 1a). We did not pursue the structure determination of this species because: (i) these fibrils appear extremely thin and bent, making them unsuitable for cryo-EM structure determination; (ii) the abundance of thick fibrils made it challenging to select these thin fibrils during particle picking.

Atomic model building

The final map of the thin fibrils was sharpened with phenix.auto_sharpen[28] at a resolution cutoff of 3.7 Å. The initial model was generated using ModelAngelo[29] with the αA-crystallin R116C sequence provided. Residues 50-80 were automatically built into the map by ModelAngelo, and the fibril core was extended to residues 21-89 by manually adding residues using COOT[30]. The resulting model fits the cryo-EM density unambiguously for all side chains, suggesting the correct registration of the model. The model was then extended to 6 layers and refined using phenix.real_space_refine[31] and ISOLDE[32]. The final model was validated using MolProbity[33].

Reporting summary

Further information on research design is available in the Nature Portfolio Reporting Summary linked to this article.

Data availability

Cryo-EM map and atomic model of human αA-crystallin fibrils present in this study have been deposited into the Worldwide Protein Data Bank (wwPDB) and the Electron Microscopy Data Band (EMDB) with accession codes PDB 9U4L and EMD-63849. The original data of the ThT assays displayed in Fig. 1g are provided in Supplementary Data 1. Any other relevant data are available from the corresponding author upon reasonable request.

Received: 3 April 2025; Accepted: 25 July 2025;
Published online: 06 August 2025

References

1. Bassnett, S. Lens organelle degradation. *Exp. Eye Res.* **74**, 1–6 (2002).
2. Delaye, M. & Tardieu, A. Short-range order of crystallin proteins accounts for eye lens transparency. *Nature* **302**, 415–417 (1983).
3. Moreau, K. L. & King, J. A. Protein misfolding and aggregation in cataract disease and prospects for prevention. *Trends Mol. Med.* **18**, 273–282 (2012).
4. Alperstein, A. M., Ostrander, J. S., Zhang, T. O. & Zanni, M. T. Amyloid found in human cataracts with two-dimensional infrared spectroscopy. *Proc. Natl. Acad. Sci.* **116**, 6602–6607 (2019).
5. Goldstein, L. E. et al. Cytosolic beta-amyloid deposition and supranuclear cataracts in lenses from people with Alzheimer's disease. *Lancet Lond. Engl.* **361**, 1258–1265 (2003).
6. Meehan, S. et al. Amyloid fibril formation by lens crystallin proteins and its implications for cataract formation. *J. Biol. Chem.* **279**, 3413–3419 (2004).
7. Shroff, N. P., Cherian-Shaw, M., Bera, S. & Abraham, E. C. Mutation of R116C results in highly oligomerized alpha A-crystallin with modified structure and defective chaperone-like function. *Biochemistry* **39**, 1420–1426 (2000).
8. Meehan, S. et al. Characterisation of amyloid fibril formation by small heat-shock chaperone proteins human alphaA-, alphaB- and R120G alphaB-crystallins. *J. Mol. Biol.* **372**, 470–484 (2007).
9. Cao, Q., Boyer, D. R., Sawaya, M. R., Ge, P. & Eisenberg, D. S. Cryo-EM structures of four polymorphic TDP-43 amyloid cores. *Nat. Struct. Mol. Biol.* **26**, 619–627 (2019).
10. Wang, L.-Q. et al. Cryo-EM structure of an amyloid fibril formed by full-length human prion protein. *Nat. Struct. Mol. Biol.* **27**, 598–602 (2020).
11. Kaiser, C. J. O. et al. The structure and oxidation of the eye lens chaperone αA-crystallin. *Nat. Struct. Mol. Biol.* **26**, 1141–1150 (2019).
12. Scheres, S. H. W., Ryskeldi-Falcon, B. & Goedert, M. Molecular pathology of neurodegenerative diseases by cryo-EM of amyloids. *Nature* **621**, 701–710 (2023).
13. Schweighauser, M. et al. Structures of α-synuclein filaments from multiple system atrophy. *Nature* **585**, 464–469 (2020).
14. Arseni, D. et al. TDP-43 forms amyloid filaments with a distinct fold in type A FTLD-TDP. *Nature* **620**, 898–903 (2023).
15. Yang, Y. et al. Cryo-EM structures of amyloid-β 42 filaments from human brains. *Science* **375**, 167–172 (2022).
16. Lövestam, S. et al. Assembly of recombinant tau into filaments identical to those of Alzheimer's disease and chronic traumatic encephalopathy. *eLife* **11**, e76494 (2022).
17. Qi, C. et al. Tau filaments with the Alzheimer fold in human MAPT mutants V337M and R406W. *Nat. Struct. Mol. Biol*. 1–8 https://doi.org/10.1038/s41594-025-01498-5 (2025).
18. Xiang, J. et al. Development of an α-synuclein positron emission tomography tracer for imaging synucleinopathies. *Cell* **186**, 3350–3367.e19 (2023).
19. Eckert, R. pH gating of lens fibre connexins. *Pflüg. Arch.* **443**, 843–851 (2002).
20. Shelley, K. L. & Garman, E. F. Quantifying and comparing radiation damage in the Protein Data Bank. *Nat. Commun.* **13**, 1314 (2022).
21. Kim, S. et al. Hidden route of protein damage through oxygen-confined photooxidation. *Nat. Commun.* **15**, 10873 (2024).
22. Wishart, T. F. L., Flokis, M., Shu, D. Y., Das, S. J. & Lovicu, F. J. Hallmarks of lens aging and cataractogenesis. *Exp. Eye Res.* **210**, 108709 (2021).
23. Peschek, J. et al. The eye lens chaperone alpha-crystallin forms defined globular assemblies. *Proc. Natl. Acad. Sci. USA.* **106**, 13272–13277 (2009).
24. Zheng, S. Q. et al. MotionCor2: anisotropic correction of beam-induced motion for improved cryo-electron microscopy. *Nat. Methods* **14**, 331–332 (2017).
25. Rohou, A. & Grigorieff, N. CTFFIND4: Fast and accurate defocus estimation from electron micrographs. *J. Struct. Biol.* **192**, 216–221 (2015).
26. Scheres, S. H. W. RELION: Implementation of a Bayesian approach to cryo-EM structure determination. *J. Struct. Biol.* **180**, 519–530 (2012).
27. Bepler, T. et al. Positive-unlabeled convolutional neural networks for particle picking in cryo-electron micrographs. *Nat. Methods* **16**, 1153–1160 (2019).
28. Terwilliger, T. C., Sobolev, O. V., Afonine, P. V. & Adams, P. D. Automated map sharpening by maximization of detail and connectivity. *Acta Crystallogr. Sect. Struct. Biol.* **74**, 545–559 (2018).
29. Jamali, K. et al. Automated model building and protein identification in cryo-EM maps. *Nature* **628**, 450–457 (2024).
30. Emsley, P., Lohkamp, B., Scott, W. G. & Cowtan, K. Features and development of Coot. *Acta Crystallogr. D. Biol. Crystallogr.* **66**, 486–501 (2010).
31. Afonine, P. V. et al. Real-space refinement in PHENIX for cryo-EM and crystallography. *Acta Crystallogr. Sect. Struct. Biol.* **74**, 531–544 (2018).
32. Croll, T. I. ISOLDE: a physically realistic environment for model building into low-resolution electron-density maps. *Acta Crystallogr. Sect. Struct. Biol.* **74**, 519–530 (2018).
33. Chen, V. B. et al. MolProbity: all-atom structure validation for macromolecular crystallography. *Acta Crystallogr. D. Biol. Crystallogr.* **66**, 12–21 (2010).

Acknowledgements

This work was supported by the National Natural Science Foundation (NSF) of China (grant nos. 32271276) to Q.C. and STI2030-Major Projects 2022ZD0212500 to Q.C. The authors thank for cryo-EM data collection at the Instrument Analysis Center (IAC), Shanghai Jiao Tong University. The authors acknowledge the National Facility for Translational Medicine (Shanghai) for support.

Author contributions

M.S. purified αA-crystallin protein and prepared αA-crystallin fibrils. M.S. and J.H. prepared EM samples and performed EM observation. M.S. performed the fibril stability assays. M.S. and Q.C. performed cryo-EM data collection and processing. M.S. and Q.C. built the model and analyzed the structure. All authors analyzed the results and wrote the manuscript. Q.C. supervised the project.

Competing interests

The authors declare no competing interests.

Additional information

Supplementary information The online version contains supplementary material available at https://doi.org/10.1038/s42004-025-01637-5.

Correspondence and requests for materials should be addressed to Qin Cao.

Peer review information *Communications Chemistry* thanks Sofia Lövestam and the other, anonymous, reviewers for their contribution to the peer review of this work. Peer reviewer reports are available.